CONSTRAINING THE HIGH DENSITY NUCLEAR SYMMETRY ENERGY WITH PIONS

By

Justin Estee

A DISSERTATION

Submitted
to Michigan State University
in partial fulfillment of the requirements
for the degree of

Physics – Doctor of Philosophy

2020

ABSTRACT

CONSTRAINING THE HIGH DENSITY NUCLEAR SYMMETRY ENERGY WITH PIONS

By

Justin Estee

ACKNOWLEDGEMENTS

Your acknowledgements here.

TABLE OF CONTENTS

LIST OF TABLES

LIST OF FIGURES

CHAPTER 1

INTRODUCTION

Rutherford discovered in 1911 that the atomic nuclei are composed of a dense nucleus surrounded by an electron cloud, and eventually that the nucleus if composed of positive and neutral spin 1/2 particles called protons and neutrons. The proton and neutron are actually composed of 3 fundamental particles called quarks. Besides for the charge differences between protons and neutrons, they exhibit a fundamental symmetry which explains their almost identical mass. Typically neutrons and protons are treated as two different isospin projections of a "nucleon", (-1/2 and 1/2) respectively.

The nucleus itself accounts for 99.9% of the mass of the atom and only 10^{-12} of the total volume, making it incredibly dense. Without a balancing force the Coulomb force between protons would render the nucleus unstable. The nuclear strong interaction is the fundamental force governing the interactions between the constituent quarks in the nucleons, deriving its name from the large force which acts only over small distances. The strong force is attractive only for a small regions approximately 1 fm to 2 fm and becomes very repulsive at even shorter distances. It is for this reason that the distance between nuclei is a near constant value, and therefore the density is remarkably constant over a wide range of nuclei CITE HERE. This density is referred to as the *saturation density*, $\rho_0 = 1.7 \times 10^{14} \, \mathrm{g \, cm^{-3}}$ or $0.16 \, \mathrm{fm^{-3}}$.

In this way nuclei can be thought of as an in-compressible liquid. This picture was remarkably successful at describing the binding energies of nuclei at saturation density. The Bethe-Weizsacker semi-empirical formula [1], predicts the binding energy as a function of the number of neutrons N, protons Z, and total nucleons $A = Z + N$, where the binding energy per nucleon is ϵ/A:

$$\frac{\epsilon}{A} = a_v A - a_s A^{2/3} - a_c \frac{Z^2}{A^{1/3}} - a_A \frac{(N-Z)^2}{A} + ... \tag{1.1}$$

Since the number of nucleons is related to the volume of the nucleus, the volume term ,a_V, originates from the the saturation of the strong force and its short range nature. There are correction

terms accounting for the surface, a_s, since nucleons near the surface do not have as many neighbors as nucleons inside, and the coulomb term which is related to the size of the nucleus which scales as $A^{1/3}$. The asymmetry term, a_A, is related to the cost in energy one pays to become more neutron or proton rich; it is typically referred to as the *Symmetry Energy*. This originates from pauli blocking where it is more energetically favorable to form neutron-proton pairs since their isospin numbers are different. The di-neutron and di-proton form part of the isospin triplet only allowing for the total isospin $T = 1$, where as the deuteron (neutron-proton) system may form $T = 0, 1$ in the singlet or the triplet, with the singlet being more energetically favorable.

Large macroscopic objects such as neutron stars are composed of mostly pure neutron matter CITE HERE, which is normally not stable. The large extent of the star allows for the gravitational force to balance the strong force creating a compact dense star. The pressures vary in the neutron star from low densities near the crust to the dense interior which can reach up to $9\rho_o$ CITE HERE. To understand these exotic systems, the energy density of the system must be described in a more general way than Eq. 1.1 to describe matter over a wide range of densities.

Guided by Eq. 1.1, we can separate the energy density E of a system into two components,

$$E(\rho, \delta) = E(\rho) + S(\rho)\delta^2, \tag{1.2}$$

where $E(\rho)$ describes the symmetric term (i.e. independent of isospin), and the symmetry energy $S(\rho)$ which depends on the asymmetry of the system, written now in terms of the neutron and proton densities,

$$\delta = \frac{\rho_n - \rho_p}{\rho}. \tag{1.3}$$

The Equation of State (EoS) of nuclear matter can be calculated by,

$$P = \left(\frac{\delta E}{\delta V}\right)|_{T=0,N} = -\rho^2 \frac{\delta E}{\delta \rho}|_{T=0,N}, \tag{1.4}$$

for a fixed number of particles N and zero temperature. One can extend to higher temperatures by adding the Boltzman dependence. The partial derivative with respects to volume can be rewritten in terms of density:

$$P = -\rho^2 \frac{\delta E}{\delta \rho}|_{T=0,N}.$$ (1.5)

To understand macroscopic pressures in the neutron star, which balance the gravitational force, we must understand the density dependence of the symmetry energy.

1.1 Density Dependence of the Symmetry Energy

In the last couple decades, the symmetric term of Eq. 1.2 has been determined for a wide range of densities ranging from $\rho_0 - 9\rho_0$ CITE HERE. In contrast, the symmetry energy has only been experimentally constrained for densities at or below ρ_0. Figure 1.1 shows some of the experimental constraints which have been performed by a series of independent measurements and observables CITE HERE ALL. Typically an effective interaction is used to describe the phenomenological observations of nucleon-nucleon interactions observed in nuclei. One of such interactions is described by the Skyrme interaction, which typically is described by a multi-parameter function which takes into account momentum dependence (through an effective mass), 2-body interactions, and correlations [3]. Several Skyrme parameterizations are shown as lines in Fig. 1.1. Though most of the functional forms satisfy the experimental constraints at low densities there is a considerable uncertainty at high densities, which are more relevant to neutron stars.

1.2 Heavy Ion Collisions

Besides observing neutron stars directly, heavy-ion collisions (HIC) provide the only way we can probe the density dependence of the symmetry energy in the laboratory setting. When two nuclei collide in a collision, in the very early stages they compress to form a high density region where

the nuclei overlap. This momentary density can reach up to $3\rho_0$ depending on the incident beam energy. HICs provide the only way we can probe the isospin asymmetry dependence of the nuclear EoS. This is accomplished by using radioactive neutron-rich beams to collide on stable targets.

The pressure arising from the symmetry energy depends on the curvature of the symmetry energy at a given density. If the density dependence of the symmetry energy is positive at high densities the symmetry energy would work to force neutrons out of the system. Where as if the derivative was negative the symmetry energy would attract neutrons. It is this pressure that is driving the dynamics of neutrons and protons. By measuring protons and neutrons we can see signatures of the effects of the symmetry energy in the final spectra of these particles. Measuring neutrons experimentally can be quite challenging and space is limited by large neutron wall arrays. Also, though the overlap region temporarily reaches a high density, the neutrons which participated in this region also evolve through regions of lower densities until they reach their final state, diluting the signal from the dense region.

1.3 Pion Observable

It is preferable to find an observable that is easier to measure experimentally than neutrons, and is more sensitive to the high density region. Pions are produced though and intermediate process where nucleon-nucleon collisions form an excited $\Delta(1232)$ baryon resonance from one of the nucleons, which then decay decay shortly after into a pion:

$$NN \rightleftharpoons \Delta N \rightleftharpoons \pi NN. \tag{1.6}$$

The threshold for Δ resonance production, with a mass of $1232\,\mathrm{MeV}\,c^{-2}$, corresponds to a laboratory beam of $290\,\mathrm{MeVA}$ kinetic energy. In large nuclei the nucleons exist in orbitals which have large amounts of energy (Fermi energy), allowing for Δ production even at sub-threshold beam energies [4].
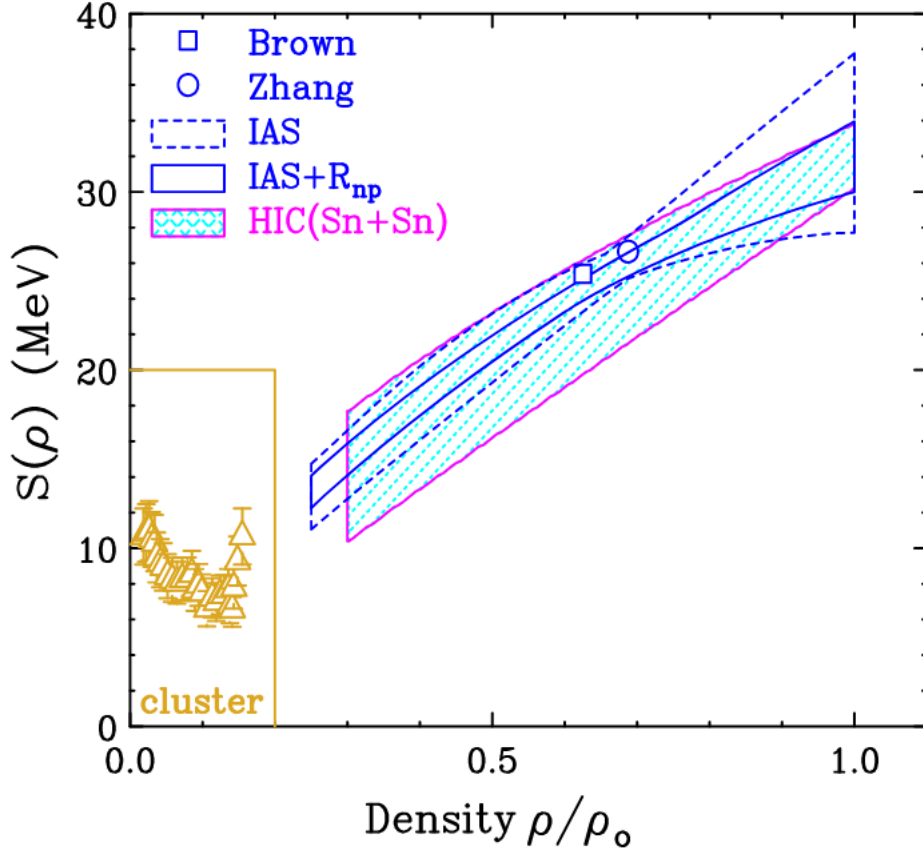
Figure 1.1: Experimental constraints of the density dependence of the symmetry energy taken from [1]

It has been shown in [2] that most of the Δ's are produced in the early dense regions of the collision. Figure 1.2 shows the average local density (c) which Δ's are produced and the number in the system (b), as a function of time in the simulation of Au + Au collisions at $400\,\mathrm{MeVA}$. Panel (a) shows the density distribution of the density at the moment of creation for Δ's. Since the average lifetime of the Δ is $\tau_\Delta = 1.7\,\mathrm{fm}\,c^{-1}$, the Δ resonance has very little time to be affected by the medium before decaying into a π and nucleon. Thus the outgoing π is contains information on the high density region of the collision.

The branching ratio of the various flavors of Δ's is given by the Clebsh-Gordon coefficients as shown in A.0.1. Here we see that in general proton-proton collisions give rise primarily to π^+ and
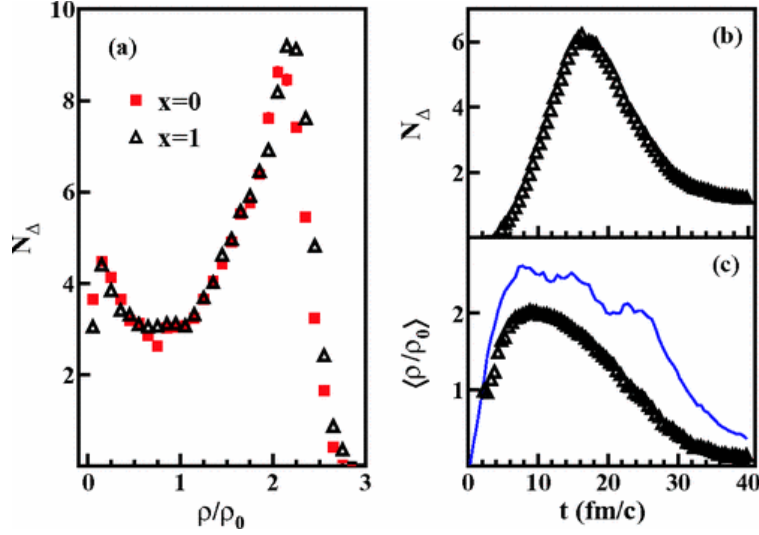
Figure 1.2: Figure taken from [2] for Au + Au collisions at 400 MeVA. Panel (a) shows the density in the region of the Δ resonance creation for two different symmetry energies (x=0 soft) and (x=1 stiff). Panel (b) and (c) show the evolution of collision in time steps, where (b) shows the number of deltas in the system as a function of time and (c) shows the mean local baryon density in the region where Δ resonances are produced. The blue line in (c) represents the average baryon density in the most central region of the collision. This evidence shows that a majority of Δ's are produced in the high density region of the early collision.

neutron-neutron collisions give rise to primarily π^-. In this Δ resonance model the charged pion ratio can be described as,

$$\frac{\pi^-}{\pi^+} = \frac{5pp + pn}{5nn + pn}. \tag{1.7}$$

In this Δ resonance model, $\pi^-/\pi^+ \approx (N/Z)^2$ where N/Z is the neutron-proton ratio of the dense central collision where they are produced. Pions can be reabsorbed into a Δ resonance after colliding with the another nucleon in the froward and backwards process $\Delta \iff \pi + N$. This process generally dilutes the pion sensitivity to the high density region, since with each absorption and re-emission would change the pion dynamics or even the charge of the pion which would reflect the asymmetry at the point of creation and eventual re-emission. Total pion absorption back into two nucleons requires a three body process where a pion is absorbed creating a Δ resonance, then another nucleon must collide with the resonance to create two nucleons. Because of this, the total pion absorption (removing pions totally) is a less frequent effect than the absorption re-emission

6

process. Yet in general by measuring the π^- and π^+ is connected with n-n and p-p collisions. Instead of measuring neutrons we can measure the π^- which is much easier to measure experimentally.

1.4 Motivation for Thesis

In an effort to answer the high density behavior of the symmetry energy, we designed a new detector and a set of experiments of Sn + Sn collision utilizing inverse kinematics where the beam is made of a radio-active neutron rich beam. This allows for the neutron-proton asymmetry of the system to be changed depending on the beam. Pion production has been studied in stable beams for beam energies of 400 MeVA and above CITE HERE. Here only total pion yields were published and no pion spectra were published. The goals of this Thesis were to measure the pion spectra efficiently, to low pion energies. To do this a new Time Projection Chamber (TPC) was made, where we measured pions and light charged particles (up to Li) in neutron-rich heavy ion collisions at 270 MeVA

CHAPTER 2

RESULTS

2.1 Pion Spectra

The efficiency correction is applied track-by-track, where the efficiency of the i-th track ϵ_i is retrieved from the database, from the parameters discussed in Section **??**. The correction factor C_i is defined as,

$$C_i = \epsilon_i^{-1}. \tag{2.1}$$

Each track that is identified as a pion, is then weighted by the correction factor C_i, when filling any histogram. By using the track-by-track method, we can transform the track into any observable of interest, notably we can transform the track from the lab frame into the center-of-mass (CM) frame. Before performing the transformation to the CM system recall the beam is at a small, but non-negligible, angle in the Lab frame, see Section **??**. The beam angle for each even is measured and a rotation is applied to all the tracks in an event, to align the beam angle along the z-axis. Doing so makes the transformation into the CM system much simpler to describe. If the beam direction is defined by a unit vector $\hat{b}$, we can define the rotation that rotates the beam into the z-axis as a rotation about an arbitrary vector $\hat{v} = \hat{b} \times \hat{z}$ where the angle between the two is given by $\cos\theta = \hat{b} \cdot \hat{z}$.

Once all the events have been rotated to align with the z-axis, transforming from the Lab to the CM frame is done by a Lorentz transformation. Where the 4-momentum vector in the lab frame is defined as $\mathbf{P} = (E/c, p_x, p_y, p_z)$. Where the corresponding Lorentz transform into the CM frame along the beam (z-axis) is defined as,

$$
A = \begin{pmatrix} 1 & 0 & 0 & 0 \\ 0 & 1 & 0 & 0 \\ 0 & 0 & \gamma & -\beta\gamma \\ 0 & 0 & -\beta\gamma & \gamma \end{pmatrix}, \tag{2.2}
$$

where β, describes the velocity of the CM system, and $\gamma = \sqrt{1 - \beta^2}^{-1}$. The parameter β can be determined from the total momentum of the system in the Laboratory frame $P = \sqrt{T_P^2 - M_T^2}$ and the total energy of the system $E = T_P + M_P + M_T$ as $\beta = -P/E$, where the (-) sign denotes the correct direction for transforming from the Lab to the CM frame. The CM transformed track is defined as $p^{CM} = \mathbf{A}p^{Lab}$.
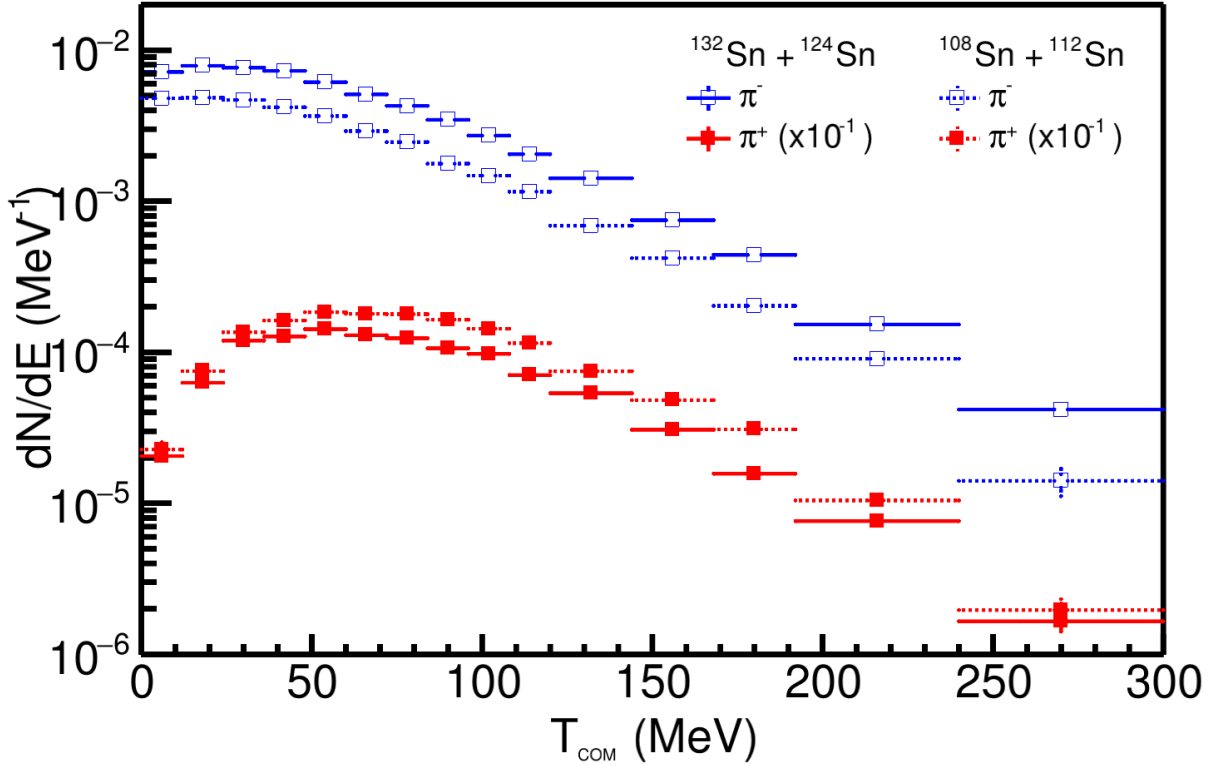

Figure 2.1: Pion spectra.

9

Figure 2.1 shows the pion CM kinetic energy spectra for both the ^{132}Sn+^{124}Sn and ^{108}Sn+^{112}Sn systems. This data marks the first pion spectral data at sub-threshold energies, extending to very low pion energies. The coulomb potential works to accelerate π^+ and decelerate π^- particles due to the positive charge of the nuclear medium. The coulomb barrier prevents the production of low energy π^+, which is why there is a reduction in the phase space around zero kinetic energy.

2.2   Comparison to Theory

Here we will compare the data with 7 different commonly used transport theoretical codes. These codes took part in a large collaboration effort to compare the codes to each other. The goal of these comparison projects was to standardize the input into each code to systematically go through the details in each code comparing things such as initialization of nuclei, stability of the code, numerical handing of pauli-blocking, etc [5, 6] CITE MORE HERE. These codes were taken in their best state, without any prior knowledge of the experimental data, and simulated the 4 systems measured in the SπRIT TPC at an impact parameter of 3 fm at 270 MeVA beam energy. Each code differs in its treatment of pion and Δ dynamics. Some codes contain modifications to the pion in nuclear matter, usually by including a pion optical potential. Some codes include the iso-scalar and the iso-vector delta potential which are not very well constrained but are important in the production of pions CITE HERE. What will be the consistent theme will be the large variation between theoretical codes. Though many of the numerical and theoretical treatments have been addressed, many of the details of pion production and dynamics have not been addressed. Though several codes show sensitivity to different symmetry energies within a particular code, the variation between codes was much larger.

2.3   Pion Yield

The integrated pion yield for both systems and the π^-/π^+ ratio is listed in Table 2.1, where the systematic errors are the first error bar and the statistical error is listed next. It is remarkable that the

System	π^-	π^+	$Y(\pi^-)/Y(\pi^+)$
^{132}Sn + ^{124}Sn	0.717(24)(4)	0.148(5)(2)	4.84(10)(6)
^{108}Sn + ^{112}Sn	0.399(14)(3)	0.200(8)(2)	1.99(4)(3)

Table 2.1: Total pion yield.

pion ratio is significantly greater than the N/Z of the system which is what is expected in the Delta Resonance model or under the assumption of chemical equilibrium which is $\pi^-/\pi^+ = (N/Z)^2$ [7, 8]; 2x in the ^{132}Sn + ^{124}Sn system and 1.4x in the ^{108}Sn + ^{112}Sn system. The pion ratio was hypothesized to be proportional to the high density N/Z ratio of the early system, where the other effects such as pion absorption and re-emission would dilute the effect and lower the ratio as the system tends toward isospin equilibrium. A naïve interpretation would be the high density N/Z fraction is much higher for some reason than the two systems, though, the system spends very little time in this state which would require a very soft Symmetry Energy. A more likely conclusion is the mechanisms involved in pion productions via the $\Delta(1232)$ resonance is more complicated than the simple $(N/Z)^2$ relation. For example the Δ resonance potential has an iso-scalar component (independent of iso-spin) and an iso-vector component. The nature of these two potentials is still unknown, and the role it plays in pion production has shown to be very important [9].

We have compared the total pion yields and ratios to the 6 common transport codes for the systems measured. The table of the transport codes are listed in Appendix A.0.3. Figure 2.2 shows the total pion yield for the four systems measured as compared with the codes. The codes plotted here are only the soft symmetry energy since the variation in code is much larger than the intra-code variation between different Symmetry Energies. While some codes make a reasonable approximation of a particular charge pion, no code reasonably predict both.

Figure 2.3 shows the total single pion ratio and the double ratio of the ^{132}Sn + ^{124}Sn and ^{108}Sn + ^{112}Sn system. Here, the variation between codes is much larger than the variation between the Symmetry Energy within a particular code. The Symmetry Energy variation of two codes – χBUU and TuQMD – is plotted as a wide band in the single ratio and all codes in the double ratio;
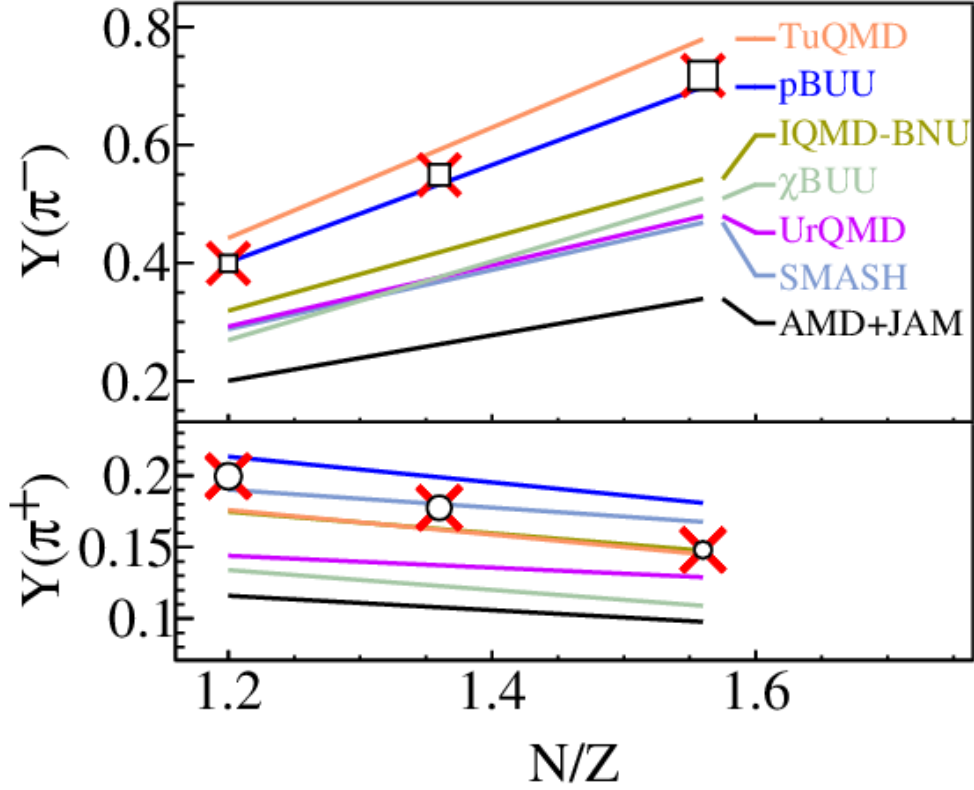
11

Figure 2.2: Total pion yields as compared with 6 common transport codes.

the data band represents the data error bar. Certainly the variation between Symmetry Energy in the ^{132}Sn + ^{124}Sn, though small, still exists in many of the codes as predicted initially [7, 8]. The small error bars in the data also would allow for a detailed analysis to extract a constraint of the Symmetry Energy, if the variation between codes could be solved.

2.4   Pion Spectral Ratio

The pion spectral ratio is a promising observable in particular it may be more sensitive to the high density regions of the early collision. In theory the high energy pions are more likely to exit the nuclear medium earlier, and therefore be less prone to effects such as pion absorption and re-emission which dilute the sensitivity of the pion observable to the high density behavior. Also low energy pions are more likely to be affected by other effects such as the Δ potential in medium [9]. If we integrate the total pion yield we combine these two regions of low and high energy
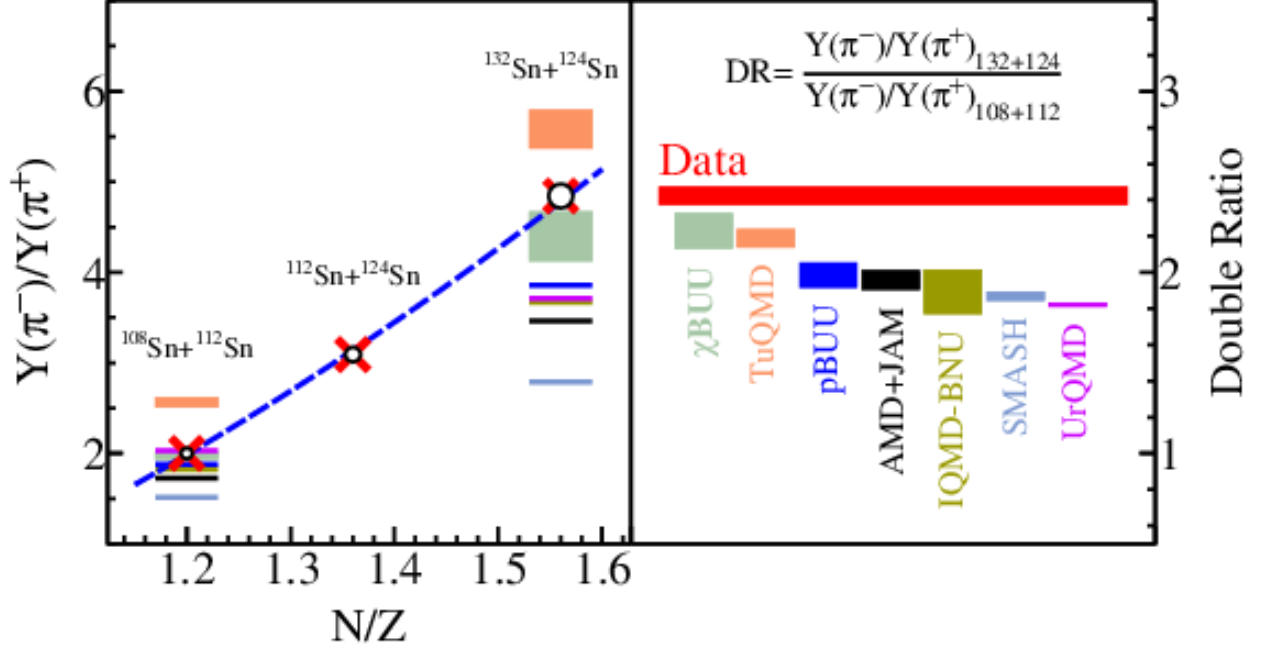
Figure 2.3: Total pion ratio and double ratio compared with 6 common transport codes.

pions. Instead we can construct the $Y(\pi^-)/Y(\pi^+)$ ratio as a function of the kinetic energy in the CM system.

Figure 2.4 shows the pion spectral ratio for both systems, which was measured with a high degree of accuracy. The general hyperbolic shape comes from the Coulomb force on the two charged pion spectra mentioned in Section 2.1. Naturally the pion ratio is smaller for less neutron poor system, i.e. less neutron-neutron collisions produce less π^-. The bin size of the last bin was increased to reduce the statistical error bars since the number of pions, especially the π^+, is reaching the limits of the measured distribution.

2.5 Pion Double Ratio

Another promising observable is the spectral double ratio. In a similar way described in Section **??** we would expect systematic uncertainties in the experiment, and even in the theory, to cancel out. For the same reasons as the pion spectral ratio, we would expect the high energy pions to be more sensitive to the high density region of the early collision.
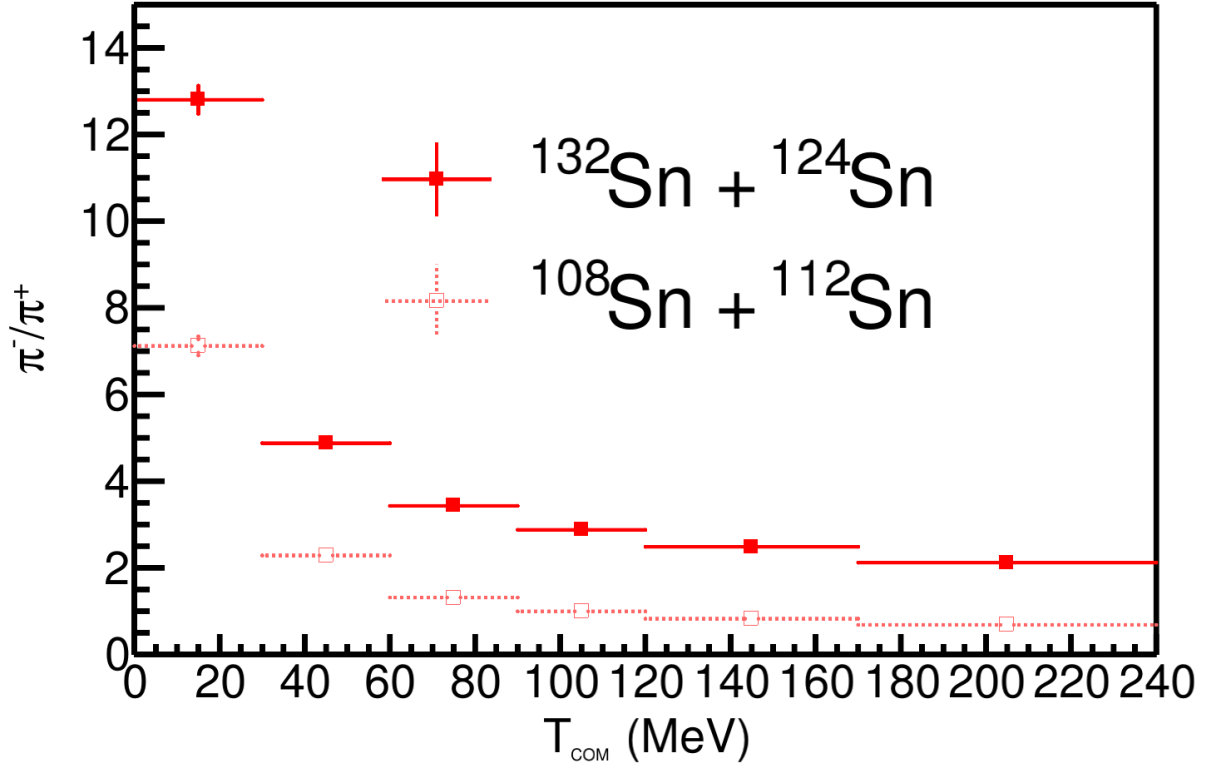
Figure 2.4: Single ratio spectra

2.6 Comparison to Previous Data Sets (FOPI)

The FOPI collaboration has measured the total pion multiplicity resulting from $^{197}Au + ^{197}Au$ collisions at several, higher beam energies. In the $^{132}Sn + ^{124}Sn$ data $N/Z = 1.56$ where as in the $^{197}Au + ^{197}Au$, $N/Z = 1.493$. The pion ratio is proportional to the N/Z of the system. Since 4 beams were measured in this experiment, the N/Z dependence was measured as seen in Fig. 2.3. Here the dependence is fitted with a 2-nd order polynomial fit. The pion ratio in the $^{132}Sn + ^{124}Sn$ data was scaled by the ratio between $N/Z = 1.56$ and 1.493. Figure 2.6 shows the scaled pion ratio as compared with the FOPI pion ratio [10]. The fitted function has the functional form of $p_1(E - p_2)^{-2}$ where p_1 and p_2 are free parameters, and is meant to guide the eye. It is worth mentioning that the pion ratio observed in the FOPI 400 MeVA setting was already considerably higher than what is expected from the $(N/Z)^2$ delta resonance model [7, 8]. Scaling the other systems in the SπRIT TPC data leads to almost the exact same value of $Y(\pi^-)/Y(\pi^+) = 4.82$.

14
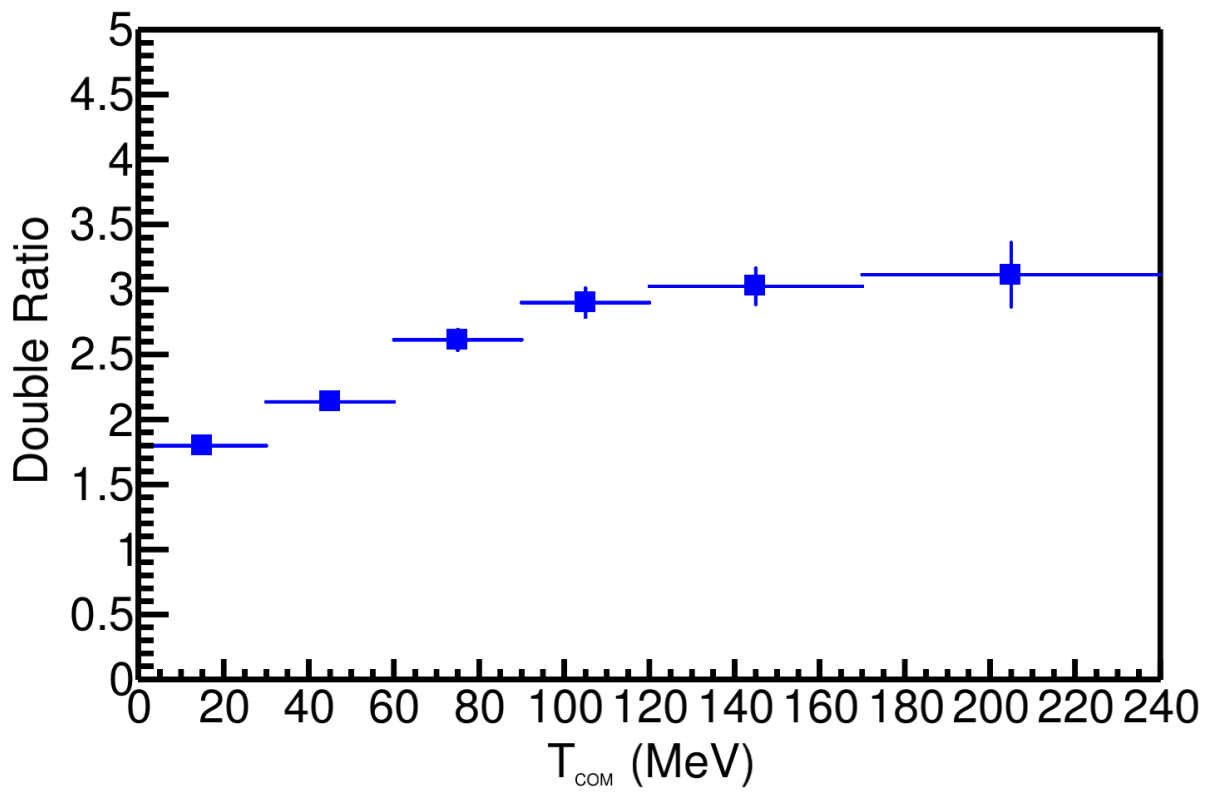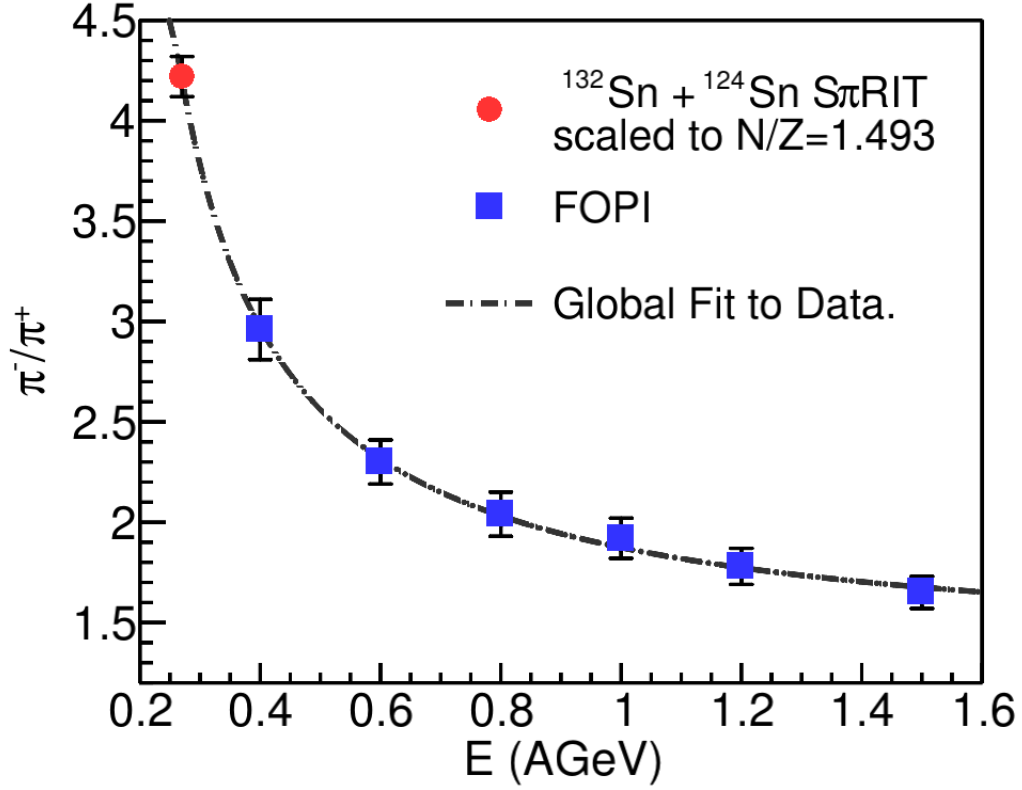
Figure 2.5

Figure 2.6: Comparing the total π^-/π^+ ratio of the ^{132}Sn + ^{124}Sn system to the ^{197}Au + ^{197}Au data from the FOPI collaboration. The SπRIT TPC data was scaled by a factor to compare to the lower N/Z of the Au + Au system. This was extracted from measuring the N/Z dependence measured in the experiment.

APPENDIX

A.0.1 Δ Resonance Production and Decay Channels

The Clebsh-Gordon coefficients for nucleon-nucleon leading to certain Δ resonances and the respective nucleon:

$$p + p \rightarrow \sqrt{\frac{3}{4}}(\Delta^{++} + n) - \sqrt{\frac{1}{4}}(\Delta^+ + p)$$

$$n + p \rightarrow \sqrt{\frac{1}{2}}(\Delta^+ + n) - \sqrt{\frac{1}{2}}(\Delta^0 + p) \tag{3}$$

$$n + n \rightarrow \sqrt{\frac{1}{4}}(\Delta^0 + n) - \sqrt{\frac{3}{4}}(\Delta^- + p)$$

A corresponding Clebsh-Gordon coefficients for the decay of Δ pions into the constituent π and corresponding nucleon:

$$p + p \rightarrow \sqrt{\frac{5}{6}}(\pi^+ + p + n) - \sqrt{\frac{1}{6}}(\pi^0 + p + p)$$

$$n + p \rightarrow \sqrt{\frac{1}{6}}(\pi^+ + n + n) + \sqrt{\frac{2}{3}}(\pi^0 + n + p) + \sqrt{\frac{1}{6}}(\pi^- + p + p) \tag{4}$$

$$n + n \rightarrow \sqrt{\frac{1}{6}}(\pi^0 + n + n) - \sqrt{\frac{5}{6}}(\pi^- + n + p)$$

Here we can see that that proton-proton collisions are connected with π^+ and neutron-neutron collisions are connected with π^-.

A.0.2 Runs analyzed in this data

System	#runs	Run numbers
^{132}Sn+^{124}Sn	113	2841, 2843, 2844, 2845, 2846, 2848, 2849, 2850, 2851, 2852, 2855, 2856, 2857, 2858, 2859, 2860, 2861, 2875, 2877, 2878, 2879, 2880, 2881, 2882, 2883, 2884, 2887, 2888, 2889, 2890, 2891, 2892, 2893, 2894, 2896, 2898, 2899, 2900, 2901, 2902, 2903, 2904, 2905, 2907, 2914, 2916, 2917, 2919, 2920, 2921, 2922, 2924, 2925, 2926, 2927, 2929, 2930, 2931, 2932, 2933, 2934, 2935, 2936, 2939, 2940, 2941, 2942, 2943, 2944, 2945, 2946, 2948, 2955, 2956, 2958, 2959, 2960, 2961, 2962, 2964, 2965, 2966, 2968, 2969, 2970, 2971, 2972, 2973, 2975, 2976, 2977, 2978, 2979, 2980, 2981, 2982, 2983, 2984, 2985, 2986, 2988, 2989, 2990, 2991, 2992, 2993, 2997, 2999, 3000, 3002, 3003, 3007, 3039
^{124}Sn+^{112}Sn	60	2542, 2543, 2544, 2546, 2547, 2548, 2552, 2553, 2554, 2555, 2556, 2557, 2558, 2559, 2560, 2562, 2563, 2564, 2565, 2566, 2567, 2568, 2569, 2570, 2571, 2572, 2573, 2574, 2575, 2578, 2579, 2580, 2581, 2582, 2583, 2584, 2585, 2586, 2587, 2588, 2589, 2590, 2591, 2592, 2593, 2594, 2595, 2596, 2597, 2598, 2599, 2600, 2601, 2617, 2618, 2619, 2620, 2621, 2622, 2623
^{112}Sn+^{124}Sn	68	3059, 3061, 3062, 3065, 3066, 3068, 3069, 3071, 3074, 3075, 3076, 3077, 3078, 3080, 3081, 3082, 3083, 3084, 3085, 3087, 3088, 3089, 3090, 3091, 3092, 3093, 3094, 3095, 3097, 3098, 3102, 3103, 3138, 3139, 3140, 3141, 3142, 3143, 3144, 3145, 3146, 3148, 3149, 3150, 3151, 3152, 3153, 3154, 3155, 3156, 3157, 3158, 3159, 3165, 3166, 3167, 3168, 3169, 3170, 3171, 3172, 3177, 3179, 3180, 3181, 3182, 3183, 3184
^{108}Sn+^{112}Sn	85	2272, 2273, 2274, 2275, 2276, 2283, 2284, 2285, 2286, 2288, 2289, 2291, 2310, 2311, 2314, 2315, 2320, 2322, 2323, 2324, 2325, 2331, 2332, 2333, 2334, 2335, 2336, 2337, 2340, 2341, 2362, 2363, 2368, 2369, 2370, 2371, 2372, 2373, 2374, 2375, 2378, 2379, 2380, 2381, 2382, 2383, 2384, 2385, 2386, 2387, 2388, 2389, 2391, 2392, 2393, 2394, 2395, 2396, 2397, 2398, 2399, 2400, 2401, 2402, 2429, 2432, 2433, 2434, 2437, 2438, 2439, 2440, 2442, 2453, 2461, 2462, 2463, 2501, 2502, 2503, 2505, 2506, 2507, 2508, 2509

Table .2: List of runs for the analysis.

A.0.3 Pion Yield Theory

| Code name	L (MeV)	(a) ^{132}Sn+^{124}Sn			(b) ^{108}Sn+^{112}Sn			$DR(\pi^-/\pi^+)$
		$Y(\pi^-)$	$Y(\pi^+)$	$SR(\pi^-/\pi^+)$	$Y(\pi^-)$	$Y(\pi^+)$	$SR(\pi^-/\pi^+)$	
χBUU	45.6	0.509	0.109	4.67	0.269	0.134	2.01	2.33
	120	0.483	0.117	4.13	0.271	0.140	1.94	2.13
TuQMD	54.6	0.779	0.145	5.37	0.442	0.176	2.51	2.14
	145	0.839	0.145	5.79	0.474	0.181	2.62	2.21
pBUU	56.1	0.698	0.181	3.86	0.401	0.213	1.88	2.05
	135	0.649	0.185	3.51	0.392	0.214	1.83	1.92
AMD+JAM	55	0.339	0.0978	3.47	0.200	0.116	1.72	2.02
	152	0.311	0.0986	3.15	0.192	0.116	1.66	1.90
IQMD-BNU	54.6	0.542	0.148	3.67	0.319	0.175	1.82	2.01
	145	0.452	0.153	2.95	0.278	0.167	1.67	1.77
SMASH	55	0.468	0.168	2.79	0.287	0.190	1.51	1.85
	152	0.479	0.163	2.93	0.292	0.188	1.55	1.89
UrQMD	46	0.479	0.129	3.71	0.292	0.144	2.03	1.83
	104	0.449	0.133	3.38	0.274	0.147	1.86	1.81

Table .3: Pion multiplicities, $Y(\pi^\pm)$, single ratios $SR(\pi^-/\pi^+)$, and double multiplicity ratios, $DR(\pi^-/\pi^+)$ from seven transport codes. Each code uses two different symmetry energy functions, with all other parameters identical in the codes.

A.1 Dalitz Decay of the π^0

A.2 Cut Variation Analysis

The particular track quality cuts described in Section **??** are there to reduced the contamination from poorly reconstructed tracks which contribute to the background in the PID spectra. The best set of values were found for all the data sets which include the charged particle multiplicity of the event, dOCA, and the number of clusters cut. By varying the cuts in both the data and the MC efficiency, we can evaluate the analysis to see if there are any systematic dependencies on the observable we plot. But varying the cuts undoutably means as the cut get tighter, and less data is included, the statistical error bar will increase making it difficult to compare to more loose cuts. This is mitigated by looking at the uncorrelated error described in [11]. Here if the systematic trend of the observable is much larger than the statistical error bars on the default cuts and the uncorrelated error bars, then there is some systematic trend that either exists due to physics or some error or miscalculation in the analysis. It is usually not recommended to estimated systematic error bars using this method, but sometimes is the only way.

Here we will discuss the particular analysis using the total pion ratio as the example. Figure **??** shows the total pion as a function of several cut variations, where one cut is varied and all the others are held constant. Three cuts are of particular interest, the event multiplicity, dOCA, and the number of cluster cut. Figure **??** shows the variation as the number of cluster cut is varied. The default cut used is > 20 clusters which is represented by the middle point. The red bars represent the statistical error of this default value. The error bars on the other points are the uncorrelated error bars as described by the prescription in [11]. Here it is clear that there is a systematic bias in the pion ratio as a function
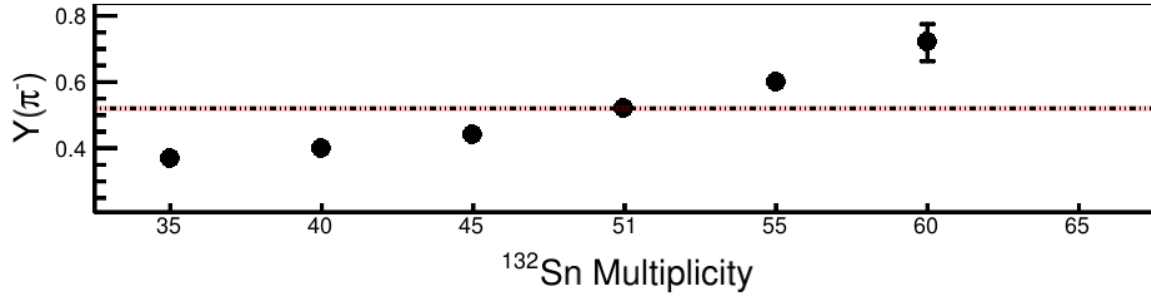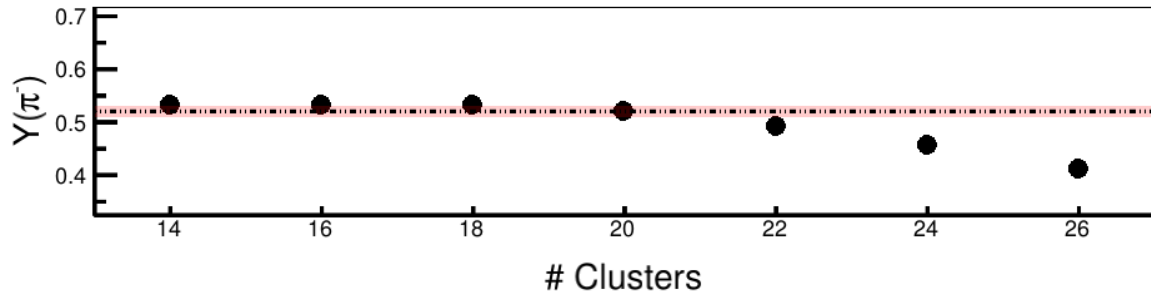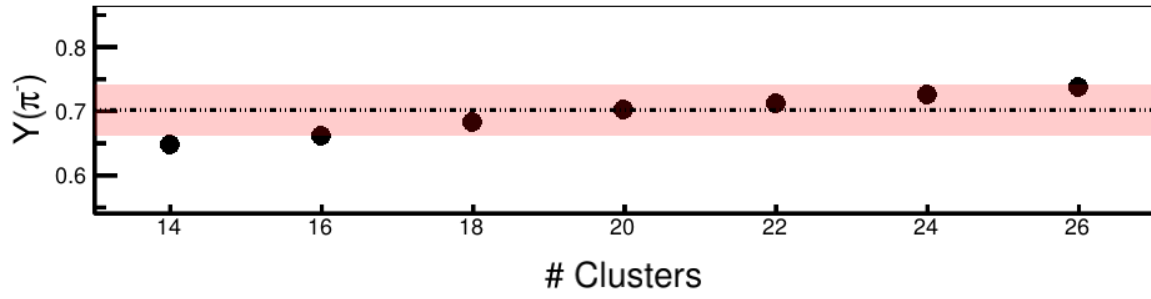
(a) No efficiency correction.
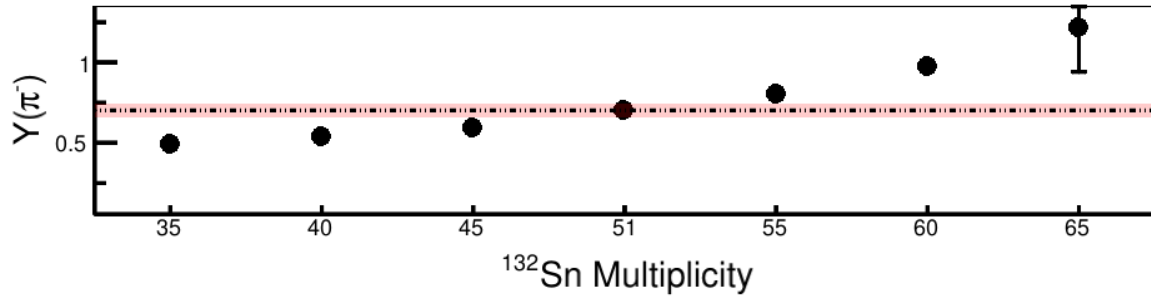
(b) Efficiency corrected.

Figure .7: $Y(\pi^-)$ when varying the ^{132}Sn charged particle multiplicity cut.
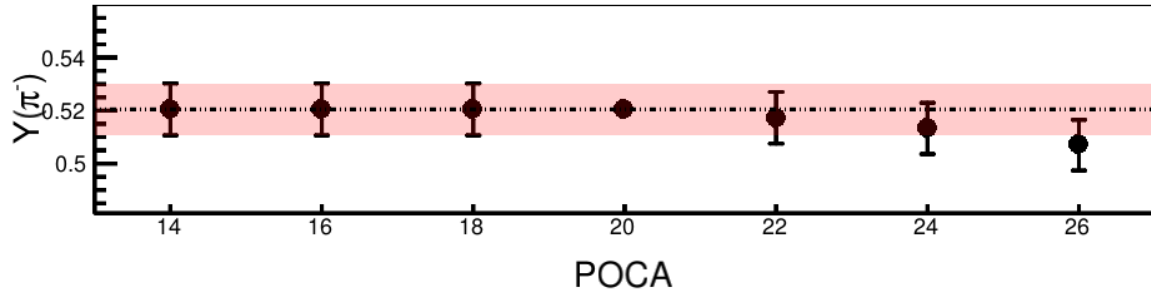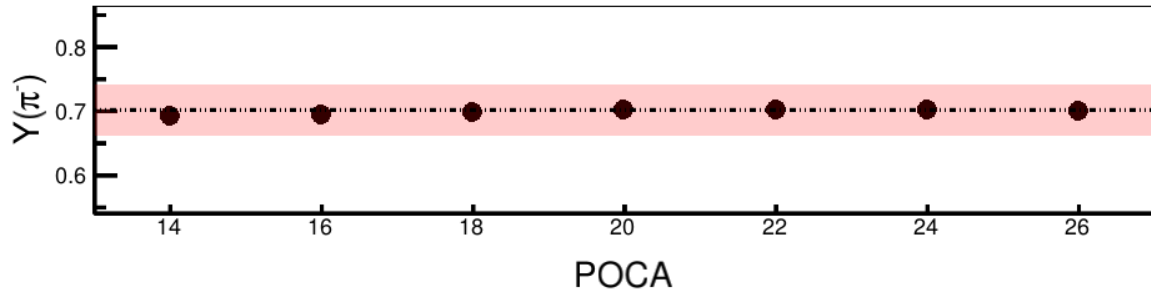
(a) Before efficiency correction.

(b) After efficiency correction.

Figure .8: $Y(\pi^-)$ when varying the number of cluster cut of the tracks.
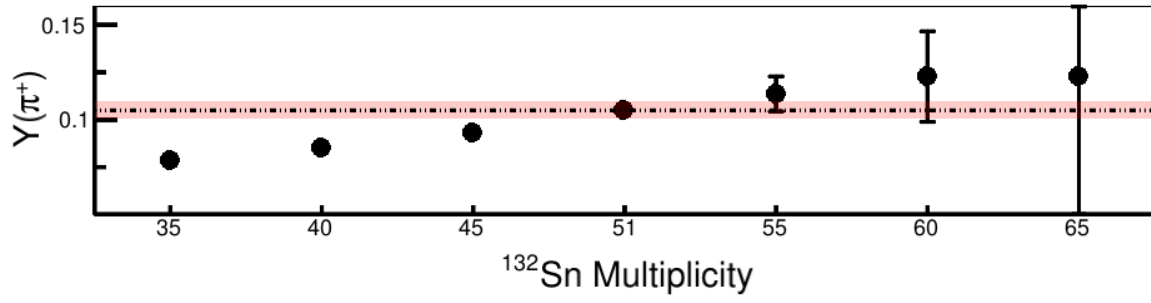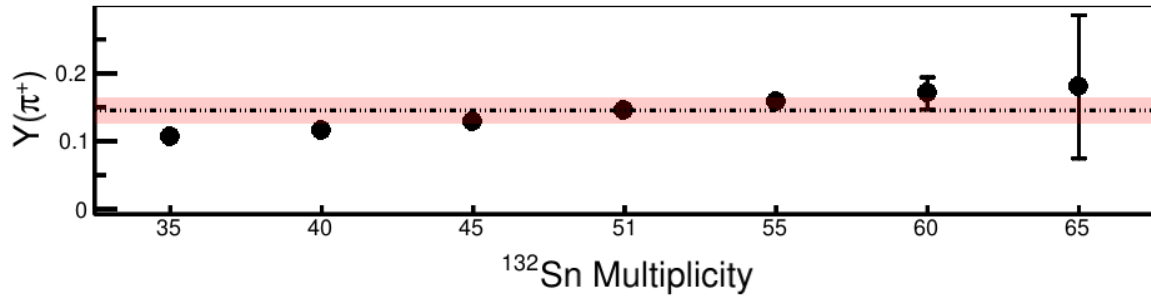
(a) No efficiency correction.

(b) Efficiency corrected.
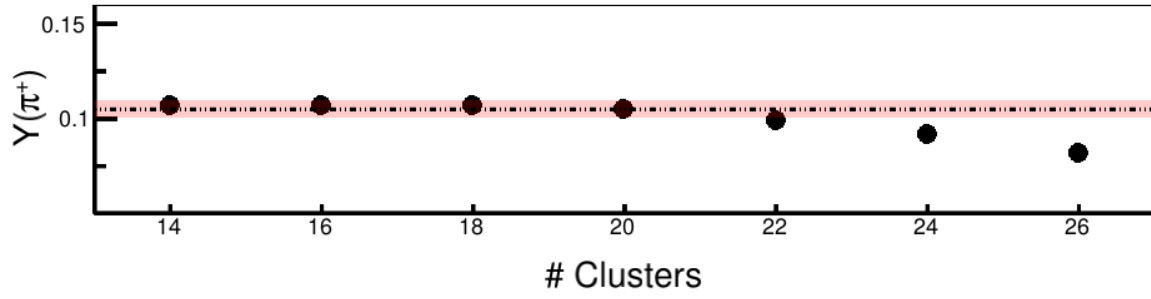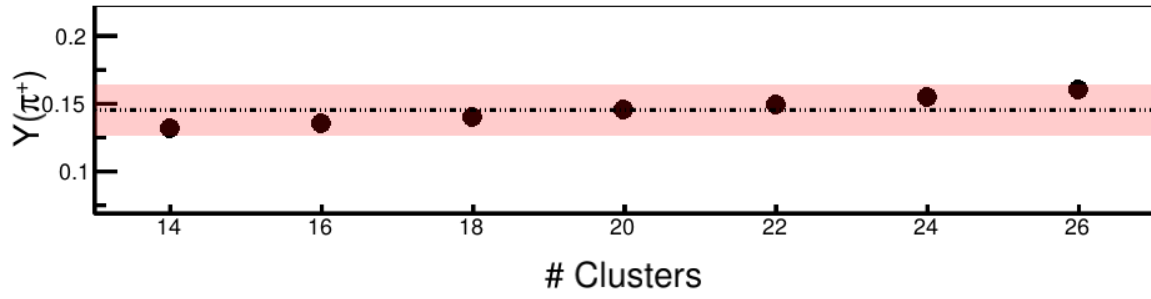
Figure .9: Y(π^-) when varying the dOCA cut.

(a) No efficiency correction.

(b) Efficiency corrected.

Figure .10: $Y(\pi^+)$ when varying the ^{132}Sn charged particle multiplicity cut.
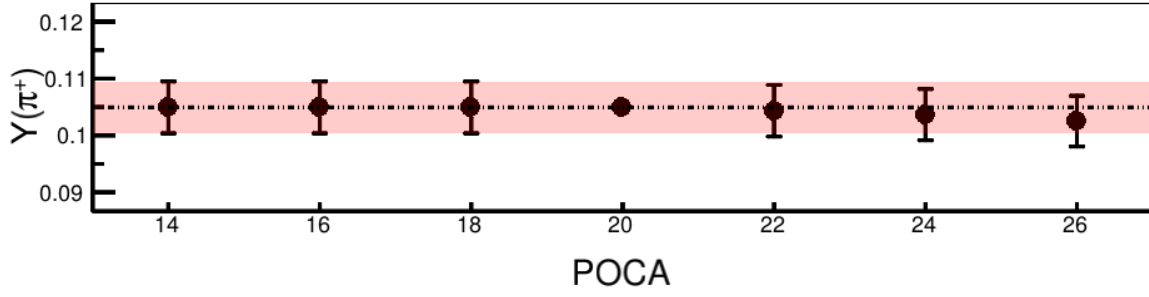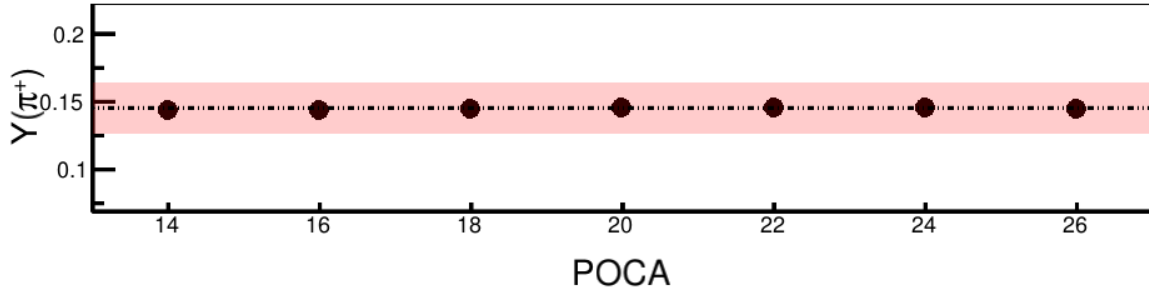
(a) Before efficiency correction.

(b) After efficiency correction.

Figure .11: $Y(\pi^+)$ when varying the number of cluster cut of the tracks.
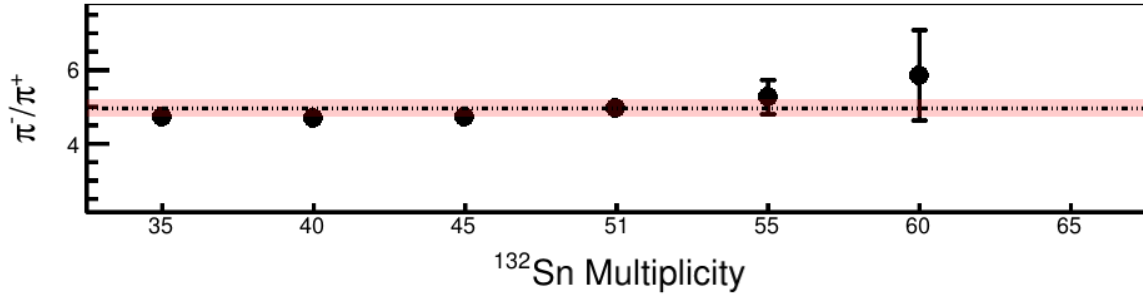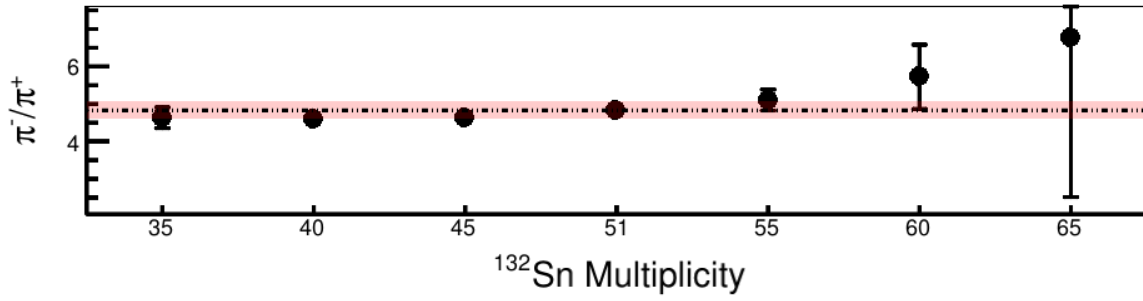
(a) No efficiency correction.

(b) Efficiency corrected.

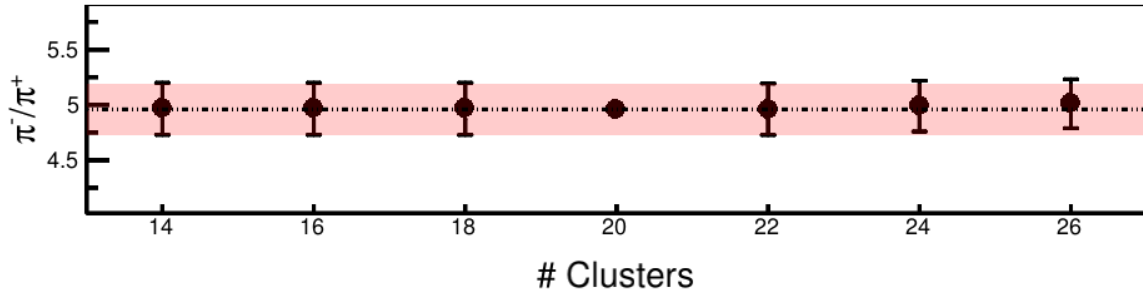Figure .12: $Y(\pi^+)$ when varying the dOCA cut.

(a) No efficiency correction.
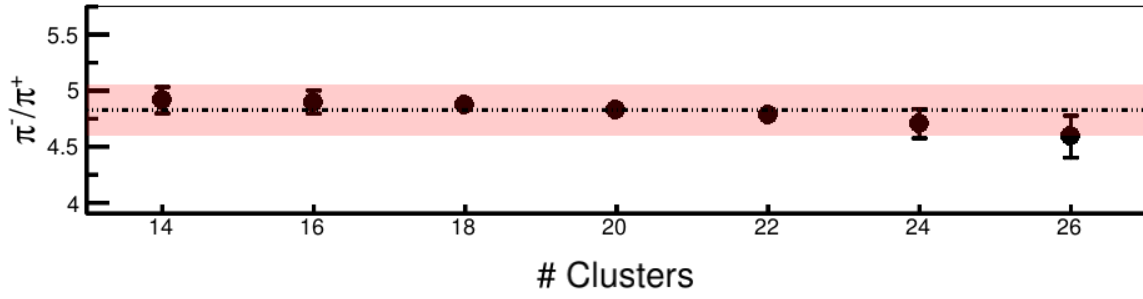

(b) Efficiency corrected.

Figure .13: $Y(\pi^+)/Y(\pi^-)$ when varying the ^{132}Sn charged particle multiplicity cut.
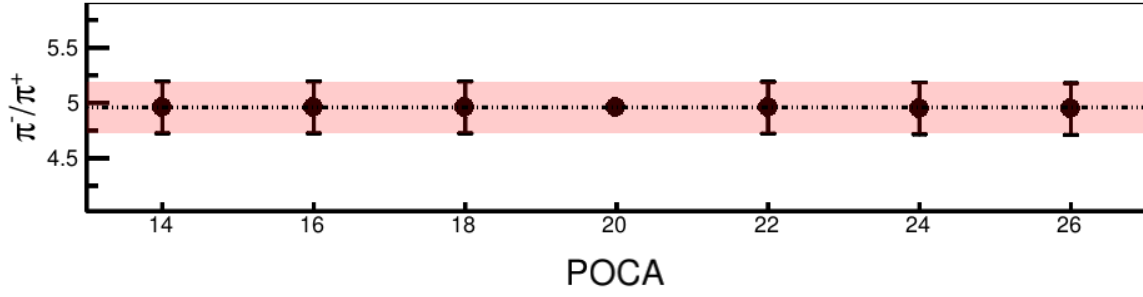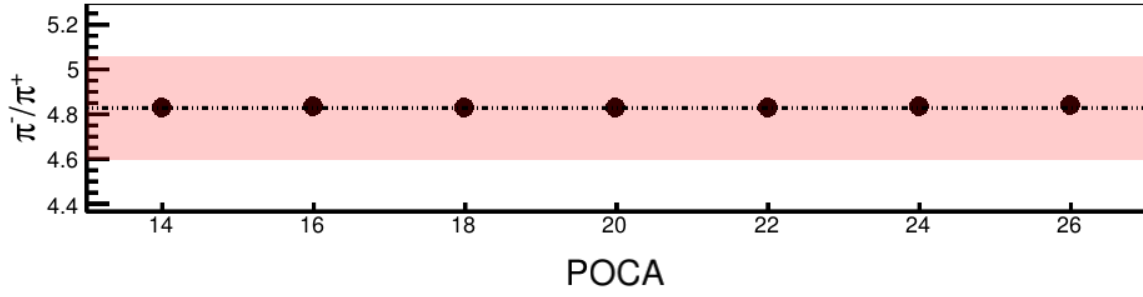
(a) Before efficiency correction.

(b) After efficiency correction.

Figure .14: $Y(\pi^+)/Y(\pi^-)$ when varying the number of cluster cut of the tracks.

(a) No efficiency correction.

(b) Efficiency corrected.

Figure .15: $Y(\pi^+)/Y(\pi^-)$ when varying the dOCA cut.

APPENDIX

SECOND APPENDIX

BIBLIOGRAPHY

BIBLIOGRAPHY

[1] C. J. Horowitz, E. F. Brown, Y. Kim, W. G. Lynch, R. Michaels, A. Ono, J. Piekarewicz, M. B. Tsang, H. H. Wolter, A way forward in the study of the symmetry energy: experiment, theory, and observation, Journal of Physics G: Nuclear and Particle Physics 41 (9) (2014) 093001.

[2] M. Zhang, Z. Xiao, B. Li, L. Chen, G. Yong, Systematic study of the π^-/π^+ ratio in heavy-ion collisions with the same neutron/proton ratio but different masses, Physical Review C 80 (2009) 034616.

[3] M. Dutra, O. Lourenco, J. Sa Martains, A. Delfino, J. Stone, P. Stevenson, Skyrme interactoin and nuclear matter constraints, Physical Review C 85 (2012) 035201.

[4] R. Stock, Particle production in high energy nucleus-nucleus collisions, Physics Reports 135 (1986) 259–315.

[5] J. Xu, et al., Understanding transport simulations of heavy-ion collisions at 100a and 400a mev: Comparison of heavy-ion transport codes under controlled conditions, Physical Review C 93 (2016) 044609.

[6] A. Ono, J. Xu, M. Colonna, P. Danielewicz, C. M. Ko, M. B. Tsang, Y.-J. Wang, H. Wolter, Y.-X. Zhang, L.-W. Chen, D. Cozma, H. Elfner, Z.-Q. Feng, N. Ikeno, B.-A. Li, S. Mallik, Y. Nara, T. Ogawa, A. Ohnishi, D. Oliinychenko, J. Su, T. Song, F.-S. Zhang, Z. Zhang, Comparison of heavy-ion transport simulations: Collision integral with pions and Δ resonances in a box, Phys. Rev. C 100 (2019) 044617.

[7] B.-A. Li, L.-W. Chen, C. M. Ko, Recent progress and new challenges in isospin physics with heavy-ion reactions, Physics Reports 464 (4) (2008) 113 – 281.

[8] B.-A. Li, Probing the high density behavior of the nuclear symmetry energy with high energy heavy-ion collisions, Phys. Rev. Lett. 88 (2002) 192701.

[9] B.-A. Li, Symmetry potential of the $\Delta(1232)$ resonance and its effects on the π^-/π^+ ratio in heavy-ion collisions near the pion-production threshold, Phys. Rev. C 92 (2015) 034603.

[10] W. Reisdorf, M. Stockmeier, A. Andronic, M. Benabderrahmane, O. Hartmann, N. Herrmann, K. Hildenbrand, Y. Kim, M. Kiš, P. Koczoń, T. Kress, Y. Leifels, X. Lopez, M. Merschmeyer, A. Schüttauf, V. Barret, Z. Basrak, N. Bastid, R. Čaplar, P. Crochet, P. Dupieux, M. Dželalija, Z. Fodor, Y. Grishkin, B. Hong, T. Kang, J. Kecskemeti, M. Kirejczyk, M. Korolija, R. Kotte, A. Lebedev, T. Matulewicz, W. Neubert, M. Petrovici, F. Rami, M. Ryu, Z. Seres, B. Sikora, K. Sim, V. Simion, K. Siwek-Wilczyńska, V. Smolyankin, G. Stoicea, Z. Tymiński, K. Wiśniewski, D. Wohlfarth, Z. Xiao, H. Xu, I. Yushmanov, A. Zhilin, Systematics of pion emission in heavy ion collisions in the 1a gev regime, Nuclear Physics A 781 (3) (2007) 459 – 508.

[11] O. Behnke, K. Kroniger, G. Schott, T. Schomer-Sadenius, Data Analysis in High Energy Physics: A Practical guide to Statistical Methods, Wiley-VCH, Weinheim, Germany, 2013.